



# **Geochemistry, Geophysics, Geosystems**

# **RESEARCH ARTICLE**

10.1002/2016GC006352

#### **Kev Points:**

- Helium release is measured real time during shale deformation using a mass spectrometer
- Helium release rate is empirically related real time to volume strain
- Release of naturally occurring helium in the subsurface may be used to monitor changes in stress, strain, and permeability in shale formations

#### Correspondence to:

S. J. Bauer, sjbauer@sandia.gov

#### Citation:

Bauer, S. J., W. P. Gardner, and J. E. Heath (2016), Helium release during shale deformation: Experimental validation, *Geochem. Geophys. Geosyst.*, 17, 2612–2622, doi:10.1002/2016GC006352.

Received 16 MAR 2016 Accepted 28 JUN 2016 Accepted article online 1 JUL 2016 Published online 16 JUL 2016

# Helium release during shale deformation: Experimental validation

Stephen J. Bauer<sup>1</sup>, W. Payton Gardner<sup>2</sup>, and Jason E. Heath<sup>3</sup>

<sup>1</sup>Geomechanics Department, MS 1033, Sandia National Laboratories, Albuquerque, New Mexico, USA, <sup>2</sup>Department of Geosciences, University of Montana, Missoula, Montana, USA, <sup>3</sup>Geomechanics Department, Sandia National Laboratories, Albuquerque, New Mexico, USA

**Abstract** This work describes initial experimental results of helium tracer release monitoring during deformation of shale. Naturally occurring radiogenic <sup>4</sup>He is present in high concentration in most shales. During rock deformation, accumulated helium could be released as fractures are created and new transport pathways are created. We present the results of an experimental study in which confined reservoir shale samples, cored parallel and perpendicular to bedding, which were initially saturated with helium to simulate reservoir conditions, are subjected to triaxial compressive deformation. During the deformation experiment, differential stress, axial, and radial strains are systematically tracked. Release of helium is dynamically measured using a helium mass spectrometer leak detector. Helium released during deformation is observable at the laboratory scale and the release is tightly coupled to the shale deformation. These first measurements of dynamic helium release from rocks undergoing deformation show that helium provides information on the evolution of microstructure as a function of changes in stress and strain.

# 1. Background

<sup>4</sup>He continuously accumulates in mineral grains and adjacent pore fluids due to alpha decay of naturally occurring U and Th. In low permeability subsurface rocks, this radiogenic <sup>4</sup>He can build up to high concentrations. The rate of transfer of helium from rock grain to the pore fluid and the transport through the rock is a function of the mineralogy, the matrix pore network distribution and fracture network, and is thus coupled to the state of stress. Changes in the distribution and release of accumulated radiogenic helium from the subsurface could provide information on changing states of stress and strain in the subsurface, perhaps allowing the development of a scheme to quantify structural evolution of shale during deformation.

Shale pore structure is hierarchical, with 100 nm pores in organic kerogen pockets and sub-micron-cracks in the inorganic complement [Loucks et al., 2009; King, 2010; Slatt and Abousleiman, 2011; Dewers et al., 2012]. The pore structure and fabric of shale and mudstone, absent of fractures, lends itself to low permeability in the  $10^{-21}$  m² range [Brace, 1980]. Kwon et al. [2004] provide a thoroughly referenced review of shale permeability indicating that laboratory measurements on shale, mudstones, and clay aggregates vary widely between  $10^{-16}$  and  $10^{-23}$  m². Permeability variations are linked to rock properties (porosity and grain size) and test stress conditions. Kwon et al. [2004] also indicate that clay content and fabric may cause anisotropy in flow properties. Grain shape alignments, which are pronounced in shales, lends to anisotropic flow properties [e.g., Bennett et al., 1989].

The variation of permeability of shales has been found to depend on porosity [e.g., *Katsube et al.*, 1991; *Dewhurst et al.*, 1998, 1999], grain size and pore distributions [e.g., *Morrow et al.*, 1984; *Dewhurst et al.*, 1998, 1999], and the hydrostatic pressure [e.g., *Morrow et al.*, 1984; *Katsube et al.*, 1991; *Dewhurst et al.*, 1998, 1999]. Permeability and anisotropy of shale decrease with increasing effective overburden pressure [e.g., *Metwally and Sondergeld*, 2011; *Kwon et al.*, 2004]. Shearing tends to decrease permeability across an experimental shear zone [*Ikari et al.*, 2009].

*Popp and Salzer* [2007] studied dilatancy in Opalinus clay and developed conceptual models relating porosity changes, stress induced deformation, permeability, and *P* wave and *S* wave velocities. Their discussion seeks to relate these independently measured physical parameters with compactive, dilatant, and failure

© 2016. American Geophysical Union. All Rights Reserved.

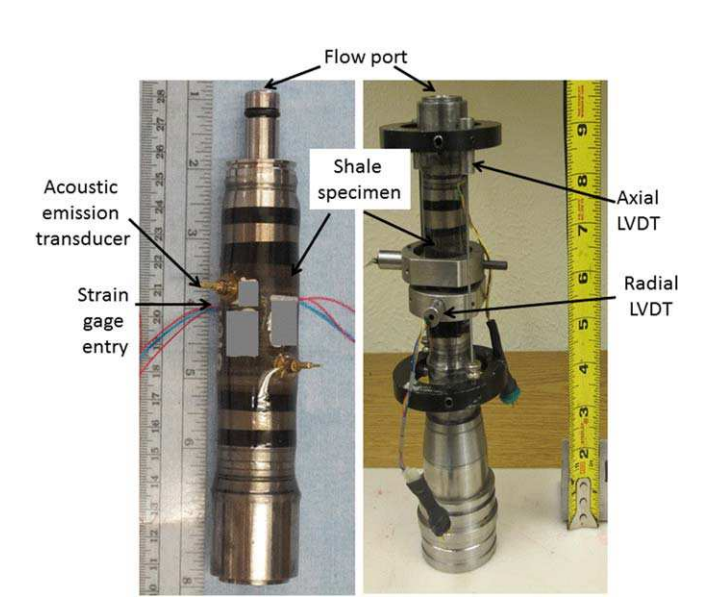


Figure 1. (left) Strain gaged sample and (right) LVDT instrumented sample.

behavior of this clay rich rock. Zhang and Rothfuchs [2008] related permeability changes in clay to the onset of dilatancy.

Nicolas et al. [2014] measured emanation of radon as a function of stress/ strain state during laboratory experiments of granite. The radon release was correlated to acoustic emissions and P wave and S wave velocity measurements and microstructural evolution. In their experiments, argon was used to flush radon from the samples at specified strain intervals. Similarly, Tuccimei et al. [2010] report on the release of radon from tuffs undergoing deformation at discrete strain intervals. Helium, as opposed to radon, is chemically inert, stable, and as a smaller molecule, more

mobile. We achieve significantly better temporal resolution with the real-time mass spectrometry measurements, as we are not limited by decay counting rates for detection. This is important in our studies because we want to directly relate helium release to deformation (volume strain).

Variation in the release of helium and other geogenic gases during rock deformation could also provide information on the evolution of microstructure and macrostructure within the rock and/or changes in the state of stress and strain. The amount of gas liberated is dependent upon the amount present and made

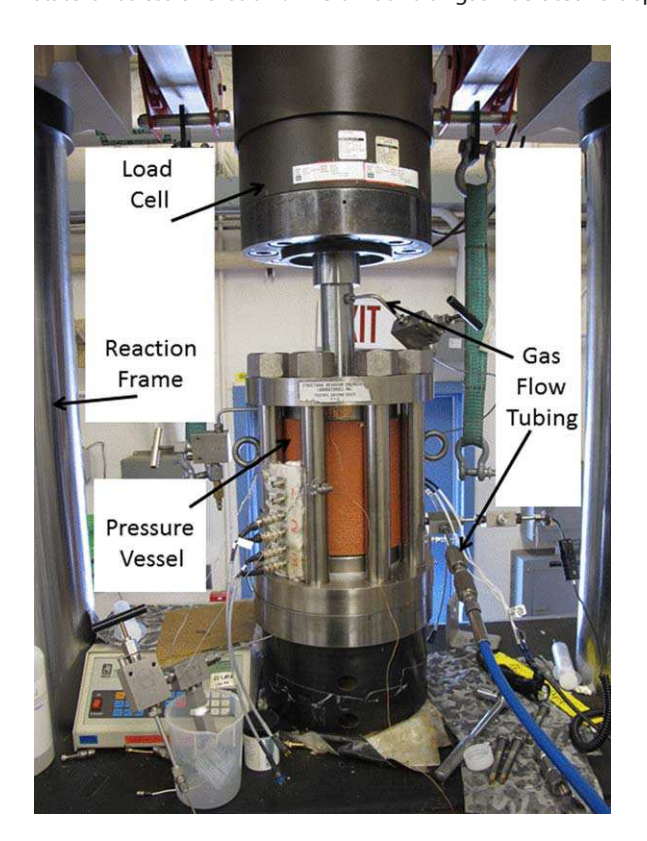


**Figure 2.** 1.0 MN testing system; reaction frame, 70 MPa pressure vessel, flow system tubing.

accessible for transport during deformation. Gas may be released during fracture and deformation due to comminution of mineral grains, liberation of gas stored along grain boundaries, diffusion from the mineral, and advection and diffusion from intact matrix to the newly formed fracture. Transfer of gas from the intact matrix to higher permeability fractures may be expected to be a function of the created fracture surface area. Transport of gas to sampling locations will be a function of the fracture network.

Here we present the first continuous observations of helium released from shale specimens undergoing deformation. Our results indicate that helium flow/release provides a sensitive measure of rock fabric evolution during deformation at the laboratory scale and could potentially provide information on changes in stress and strain in subsurface formations. Changes in helium flow in shale and or mudstone during stress evolution could be important in monitoring subsurface seals for CO<sub>2</sub> sequestration, conventional oil and gas reservoirs, compressed air storage and nuclear waste disposal, where the low shale permeability is relied upon to create a flow barrier.

# 2. Experimental Procedures

Specimens for this study were of a marine shale, and subcores were taken from 10.2 cm drill hole core. Specimens SSP1 and SSP2 are cored parallel to bedding, and SSP3 is cored perpendicular to bedding. The three specimens were located within about 10 cm of each other. The average composition of nearby shale samples is 36% clay minerals, 30% quartz, 19% calcite, 10% feldspars, and 5% other constituents. The average porosity of nearby samples is approximately 5%. These properties are considered representative of the samples used in this study.

Test specimens were 2.54 cm diameter by 5.08 cm length right circular cylinders. Specimens had a pressed metal porous frit placed on each core end to evenly distribute gas in and out of the core and were sandwiched between stainless steel end caps with pore fluid ports at the top and bottom. The end caps, frits, and core were jacketed with thin layers of paint-on, ultraviolet-cured epoxy which bonds tightly with the rock and assures intimate contact between the rock and the jacket. Helium leak blank tests using aluminum slugs of similar dimension and UV cure jacketing determined a line blank low end flow rate of approximately  $10^{-16}$  cm<sup>3</sup> STP/s.

Axial and radial displacement was recorded with a combination of resistance strain gages and/or linear variable differential transformers (LVDTs) (Figure 1). LVDT displacement measurements sample a greater volume of rock than resistance gages; however, resistance strain gages sense strain in specific locations, highlighting differences due to heterogeneous mineralogy, grain size distribution, and mechanical properties. Radial LVDTs were mounted near midheight and quarter height (Figure 1), providing two point measurements of radial displacement across the diameter. These measurements are tracked separately. Generally, the center LVDT displacement is used to calculate radial and volumetric strains. Using the radial displacement measurements, one can calculate the sample area as a function of applied pressure, allowing stresses to be calculated. Axial displacements are measured by LVDTs mounted to the specimen end caps. If two or more (redundant) displacement measurements were made, they were averaged.

Tests were performed at Geomechanics Laboratory at Sandia National Laboratories under ambient conditions ( $\sim$ 21°C and  $\sim$ 10% relative humidity). Specimens were tested in a 70 MPa pressure vessel which was placed within a 1.0 MN (225 KIP) load frame.

Jacketed specimens (Figure 1) were placed in the pressure vessel (Figure 2), the specimen/pressure vessel system was assembled and placed into the load frame, and the pressure vessel was filled with confining fluid (Isopar H<sup>®</sup>);

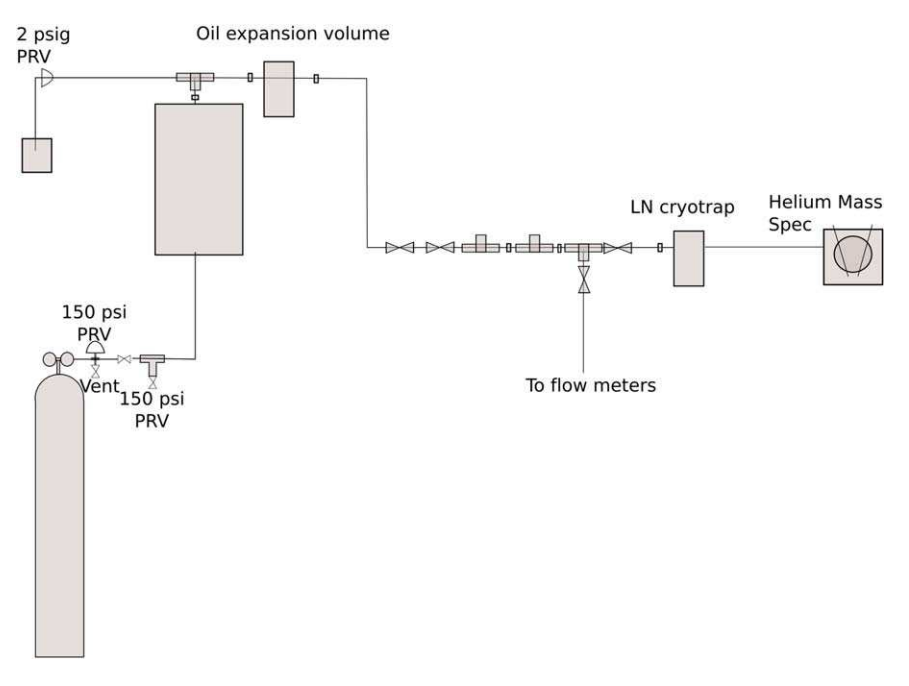
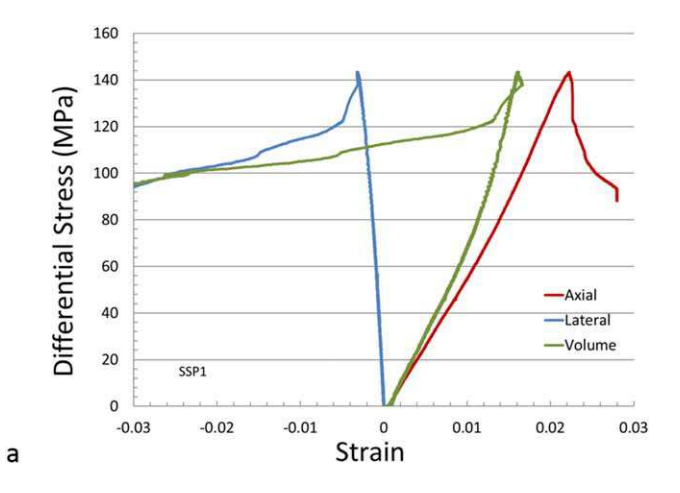
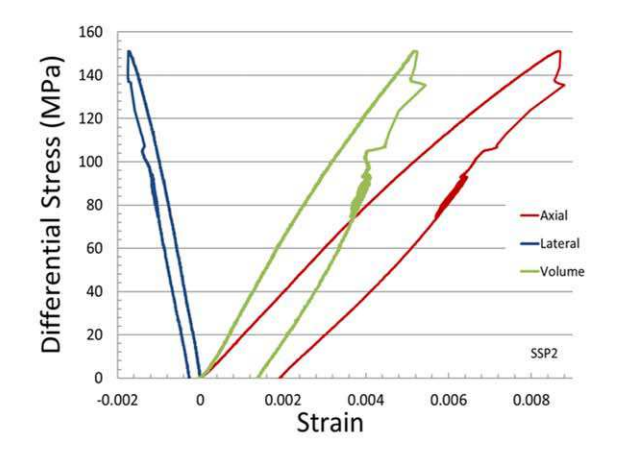
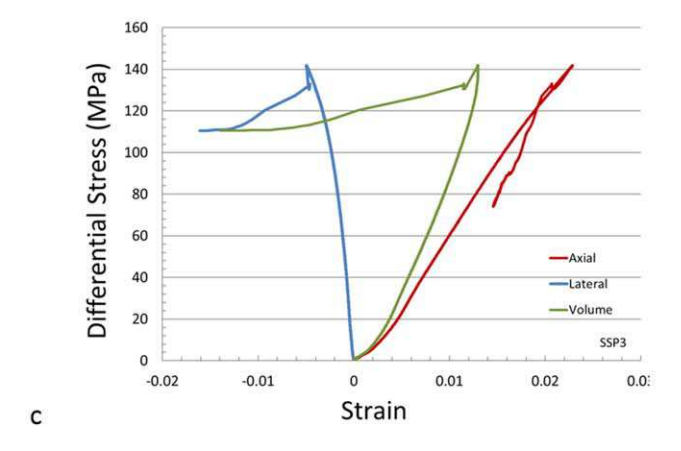


Figure 3. Helium release system schematic.

b







**Figure 4.** (a) Differential stress versus strain SSP1, (b) differential stress versus strain SSP2, and (c) differential stress versus strain SSP3.

the hydrostatic confining pressure  $(\sigma_3)$  (20.7 MPa for all tests) was then applied. Confining pressure was maintained by a servohydraulic pressure intensifier plumbed into the pressure vessel. The maximum principal stress  $(\sigma_1)$  was applied via a piston through the lid of the pressure vessel (Figure 2).

Confining pressure was controlled, measured, and tracked using a pressure transducer located in the intensifier connection line about a meter from the pressure vessel. Axial force was measured external to the pressure vessel and O-ring friction corrected for during data analysis. Specimens were deformed using a controlled displacement mode and shortened at a rate of 5  $\times$  10<sup>-6</sup> s<sup>-1</sup>. This strain rate is notably faster than tectonic strain rates and slower than earthquake seismicity and volcanic induced seismicity. Natural deformations at these or higher strain rates, locally fracturing rock, (volcanoseismic related) releases gas that has been measured [Padrón et al., 2013]. Force, displacement, confining pressure, and helium flow were recorded in an automatic data acquisition system.

Reagent grade helium was introduced to the specimen through flow ports in the end caps using O-ring connections in the end cap and pressure vessel feed-through. Swagelok VCR fittings were used for helium flow and vacuum connections outside the pressure vessel (Figure 3). This test configuration required system design and setup to accommodate physical safety and protect the high vacuum line and analytical instruments.

Vacuum line protection from jacket failure, and subsequent introduction of high pressure hydrostatic confining

fluid into the pore fluid ports, was ensured with vacuum rated, low pressure relief valves and an expansion trap capable of containing the hydrostatic fluid volume expanded from 1400 to 1 atm (Figure 3). Prior to deformation, helium was flowed through the sample for at least 24 h to enrich the pore fluid in helium as an analog of in situ reservoir conditions. The partial pressure of helium in confined shale reservoirs can be enriched more than 100 times over atmospheric partial pressure [e.g., *Gardner et al.*, 2012]. In a gas saturated reservoir this would result in a total volume of helium in the core of  $\sim$ 0.4 cm³ at 1 atm of pressure. In our cores, which have reequilibrated with the atmosphere we could expect  $\sim$ 4e<sup>-5</sup> cm³ of helium. We flowed helium at a rate of  $\sim$ 1  $\times$  10<sup>-6</sup> cm³ STP/s for 24 h as measured by our leak detector, which would

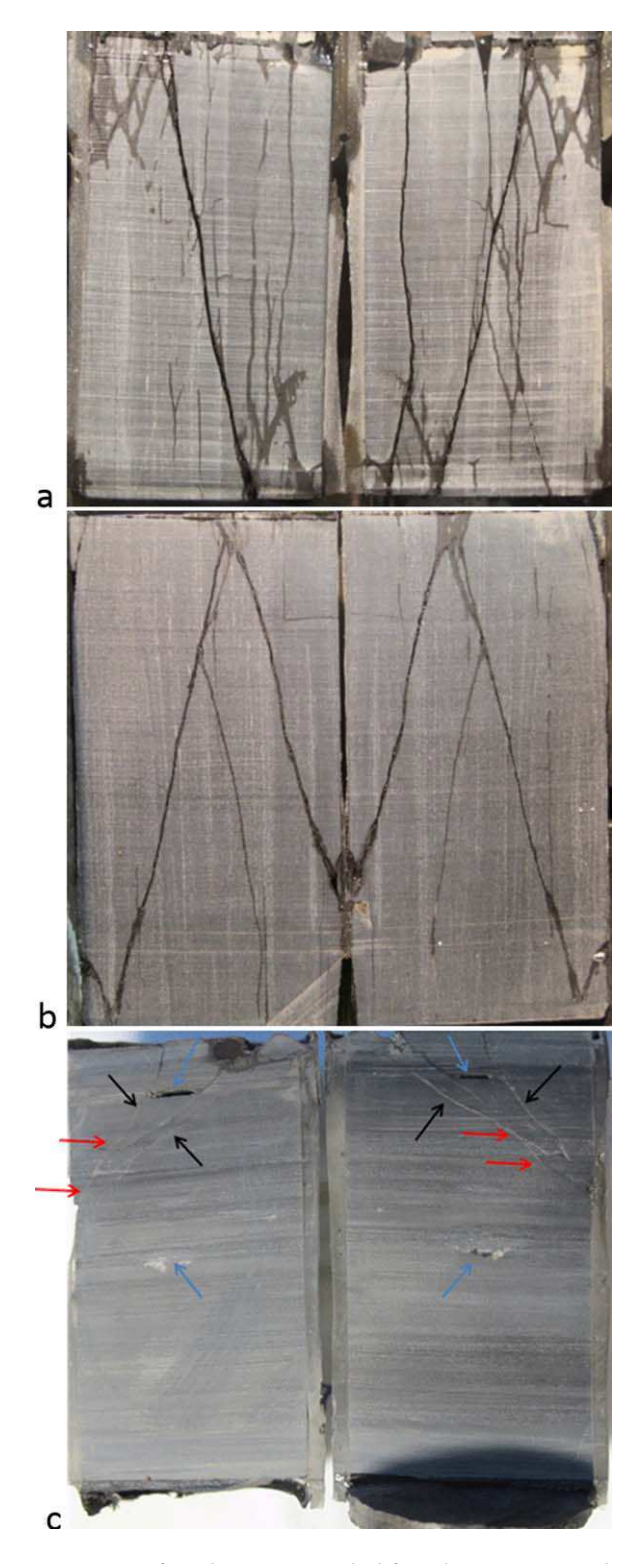


Figure 5. (a) Deformed specimen SSP1, (b) deformed specimen SSP2, and (c) deformed specimen SSP3, blue arrows point to course pockets of coarse sediment; black arrows indicate major fractures which terminate at the specimen end; red arrows point to fractures which refract (change direction) as fractures pass through fine and coarser sedimentary layers.

add a total volume of helium around 0.09 cm<sup>3</sup> STP. Thus, we significantly enriched our samples above the atmospheric value (4  $\times$  10<sup>-5</sup> cm<sup>3</sup> STP), but are still below the high end of expected reservoir conditions (0.4 cm<sup>3</sup> STP). The helium released from the sample was measured using a Leybold Phoenix L300i dry helium mass spectrometer helium leak detector [Bauer et al., 2015]. Prior to each test, the helium flow leak detector was calibrated using a calibrated standard

In this paper, we report the results of three separate helium release tests, each with different boundary conditions and/or core orientation. The three combinations of axial loading orientation (parallel versus perpendicular to bedding) and experimental boundary conditions are explained below.

Experiment SSP1: Specimen was cored parallel to bedding, and initially saturated by flowing helium through the sample at an inlet pressure of 0.345 MPa for 24 h. Prior to the start of deformation, the upstream end of the specimen was valved off, and vacuum pressure was applied to the downstream side of the specimen. As this was the first experiment, and the magnitude of the signal was not known, a  $\sim$ 5 cm<sup>3</sup> volume of pure helium at 0.345 MPa was left in the upstream tubing between the inlet valve and the top of the specimen. During the triaxial portion of the test vacuum was applied only to the downstream end of the sample; thus helium was allowed to flow from the upstream stream reservoir through the new created fractures after hydraulic connection was achieved.

Experiment SSP2: In this test the specimen was cored parallel to bedding and initially saturated by flowing helium through the sample at an inlet pressure of 0.345 MPa for 24 h. This test was designed to only measure helium released from the matrix, and no upstream helium reservoir was used. After saturation and prior to deformation, inlet pressure was relaxed to 0.1 MPa. During the triaxial portion of the test, vacuum was applied to both sides of the specimen.

Experiment SSP3: Specimen was cored perpendicular to bedding and initially saturated by flowing helium through the sample at an inlet pressure of 0.345 MPa for 24 h. After

saturation, and prior to deformation, inlet pressure was relaxed to 0.1 MPa. During the triaxial portion of the test vacuum was applied to both sides of the specimen.

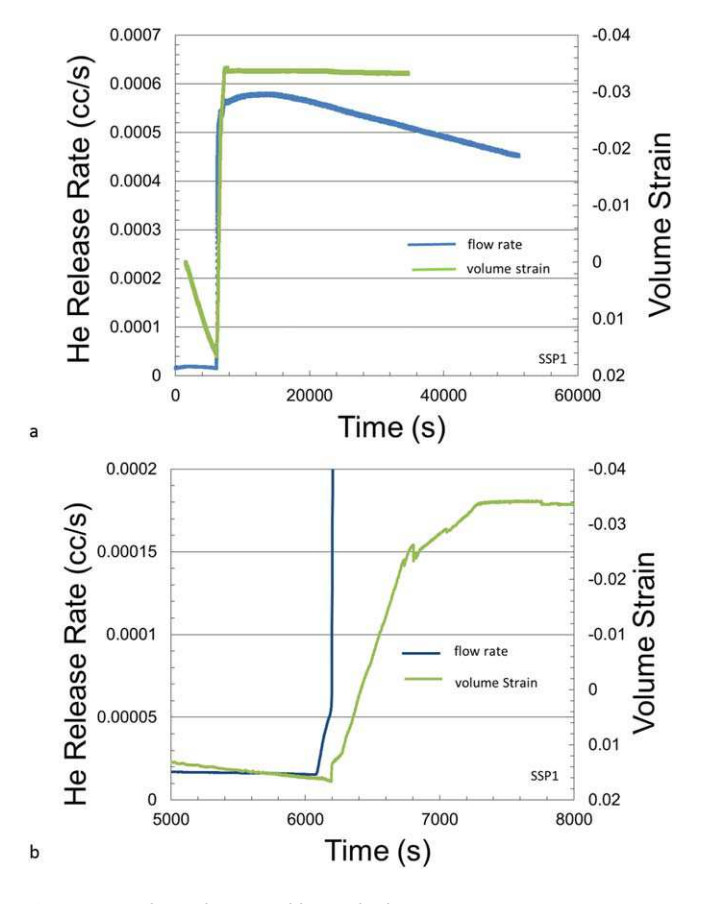


**Figure 6.** (a) Helium release rate (blue) and volume strain (green) versus time (SSP1) and (b) same data, close-up time interval.

# 3. Experimental Results

Figure 4 shows the stress-strain response for SSP1, SSP2, and SSP3. The compressive strength of the three samples is similar and ranges from 140 to 150 MPa. The axial strains vary from near 0.01 to just greater than 0.02. The effective confining pressure is essentially identical for all tests: the differences in strains are attributed to mineralogical and textural variations between specimens.

Post test observations of deformation and fractures were made on surfaces created by careful wire sawing along the long axis, perpendicular to the apparent dominant macrofractures. Within SSP1 (Figure 5a) there is pervasive fracturing in a combination of axial subparallel and low angled fractures. The fractures intersect and cross each other and strike parallel to or at small angles to bedding. Fracturing is more numerous at the specimen ends, and longer fractures terminate at the specimen ends.

For SSP2, the deformation characteristics are broadly similar to SSP1. Within SSP2 (Figure 5b) long, low angled fractures dominate. The fractures tend to

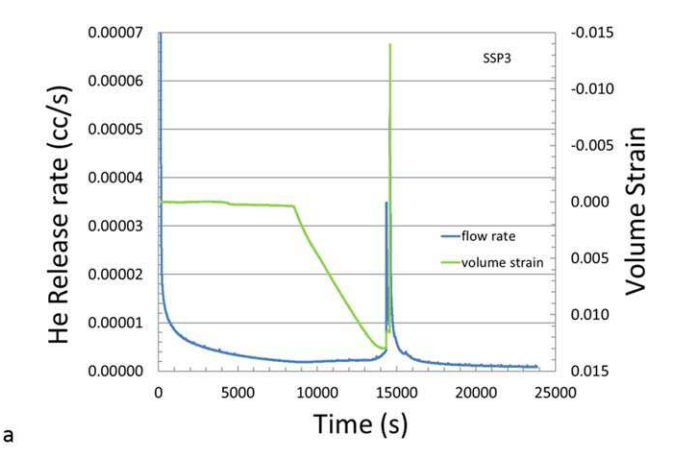
terminate at the specimen end or each other; again fractures dominantly strike at low angles to bedding. SSP2 contains fewer fractures than SSP1.

Within SSP3 (Figure 5c), the macro deformation is quite different in character to SSP1 and SSP2 and is concentrated near the specimen's top. The fractures (black arrows) terminate at the specimen's top end and along the side edge near the top, and are at a greater angle to the long axis. In close observation, it appears that fractures are lower angled near the specimen top and as they approach the side boundary. Coarse grained pockets are identified in SSP3 by blue arrows in Figure 5c, and appear to be small-scale sedimentary channels, creating minireservoirs in the rock. Sedimentary sequences produce areas of finer and coarser material in the core, which appear to have different mechanical properties represented by changes in fracture dip as the fracture transects the sample. The red arrow points to an interface between fine (above) and coarse (below) material in which the fracture angle(s) are refracted as the fracture progresses through the specimen. Fracture angles are higher in SSP3, and throughgoing fractures from one end of the sample to the other are absent. Deformation appears to be confined to the top of the sample.

#### 3.1. Flow Versus Strain Response

Volume strain and helium flow versus time are plotted in Figures 6–8. For each specimen, the first plot spans all, or nearly all, of the experiment, and the second plot spans the hour or so of intense changes in flow and deformation near the macroscopic failure point. The plots do not all start at time = zero because for some tests data collection was started before testing began. Although specimens are shortened at a relatively constant rate, displacements observed near and post failure happen quickly over a  $\sim$ 10 min interval.

The SSP1 experimental results are summarized in Figure 6. During the compressional phase of deformation, volume strain increases with time as the specimen compacts. Helium release rate (flow) decreases with time for most of this compressional stage, consistent with compaction and draining of the pore volume reservoir



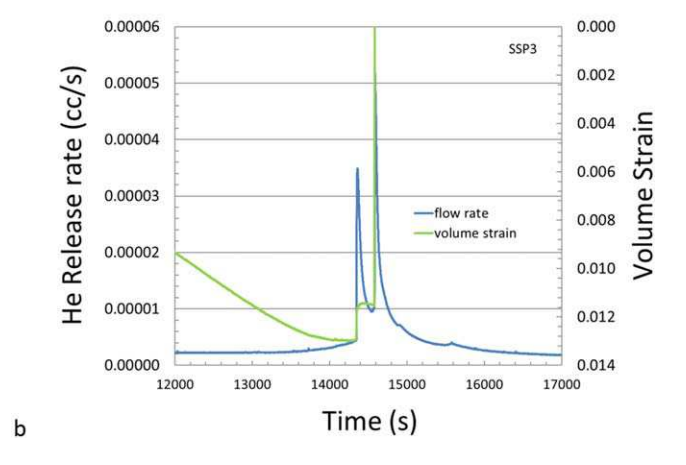


**Figure 7.** (a) Helium release rate (blue) and volume strain (green) versus time (SSP2) and (b) same data, close-up time interval.

to the vacuum. Toward the end of the compression phase a slight increase in release rate is observed. As the specimen reaches macroscopic failure, the volume strain decreases rapidly, and then levels off. This is coincident with a sharp a peak in helium flow of around  $6 \times 10^{-4} \text{ cm}^3 \text{ STP/s}$ , followed by a subsequent slow, monotonic decrease in flow. Figure 6a shows a 3000 s segment of the experiment around the fracture event. In Figure 6b, it is apparent the helium release rate increase is antecedent to macroscopic failure and that there is a rise in flow before a significant increase in volume strain is observed.

A similar pattern is observed in SSP2 (Figure 7). For early times, volume strain increases steadily with time, consistent with compaction. At 6000 s (Figure 7a), the volume strain decreases sharply (this is when the specimen loses axial strength), then increases dramatically consistent with dilation during fracturing, then levels off. Helium release decreases with increasing time during the majority of the compression phase. Between 5000 and 6000 s, the flow rate begins to increase slightly. At 6000 s, there is a sharp increase and peak flow

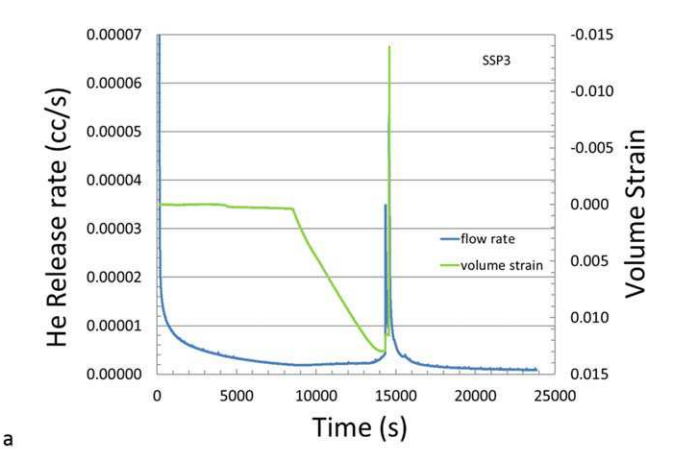
of around  $7 \times 10^{-4}$  cm<sup>3</sup> STP/s occurs followed by monotonic decrease in flow. Figure 7b shows a 4000 s segment of the experiment around the fracturing event. At 6100 s, the flow rate begins to rapidly rise, and again it is clear that flow rate begins to increase *before* macroscopic fracturing occurs (volume strain begins to decreases), implying microfracturing is occurring.

SSP3 has some of the same general characteristics of SSP1 and SSP2 but also demonstrates unique characteristics (Figure 8). Volume strain increases with increasing time (Figure 8a) as the specimen compacts until 14300 s, and then decreases abruptly to a local minimum, perhaps indicating a fracture event. The volume strain then increases slightly as the sample compresses further prior to a final decrease, indicative of a final fracture event with complete specimen failure and gage saturation. Flow decreases with time during compression until around 9000 s. Between 9000 and 14000 s, a flat or slightly increasing flow rate is observed. A sharp increase and peak in flow around  $5 \times 10^{-4}$  cm<sup>3</sup>/s occurs beginning at 14,300 s, followed by decreasing flow. At 14,600 s, a second sharp peak in flow occurs followed by monotonic decline. Figure 8b shows a 5000 s segment of the experiment around the fracturing events. The two flow rate peaks are roughly coincident with volume strain decreases.

# 4. Discussion of Results

Our experimental approach represents a new means to study the complimentary processes of deformation and flow in very low permeability rock.

Figure 9 plots strain versus helium release for SSP1, SSP2, and SSP3. For each experiment, the first phase of deformation is marked by steadily decreasing helium release, and sample compaction. In the second stage, helium flow rate begins to increase, while volume strain continues to decrease. During phase three, a rapid



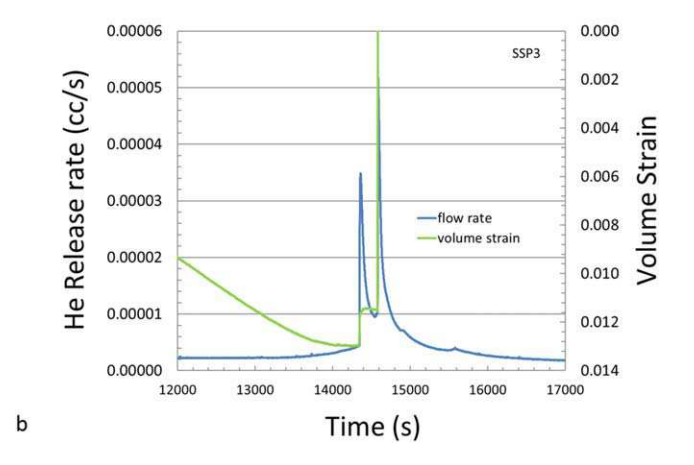


**Figure 8.** (a) Helium release rate (blue) and volume strain (green) versus time (SSP3) and (b) same data, close-up time interval.

increase in flow is coincident with a shift to dilation, with the flow rate rising faster than the dilation. Finally, the fourth stage shows continued dilation, while the flow rate stays constant (SSP1, Figure 9a) or decreases (SSP2, Figure 9b) depending upon the upstream boundary condition. In SSP3 (Figure 9c), these stages are approximately repeated in rapid succession during a second brief loading and fracturing event.

The overall trends suggest the following interpretation. The compression phase is characterized by a constant or slowly decreasing flow of helium and a constant increase in volume strain, limb 1 on the He flow versus strain plots (Figure 9). The decrease in flow rate could result from a loss in permeability due to compaction and/or from reservoir depletion. The flow rate decrease is counteracted to some extent by the release of helium from storage due to pore space compression.

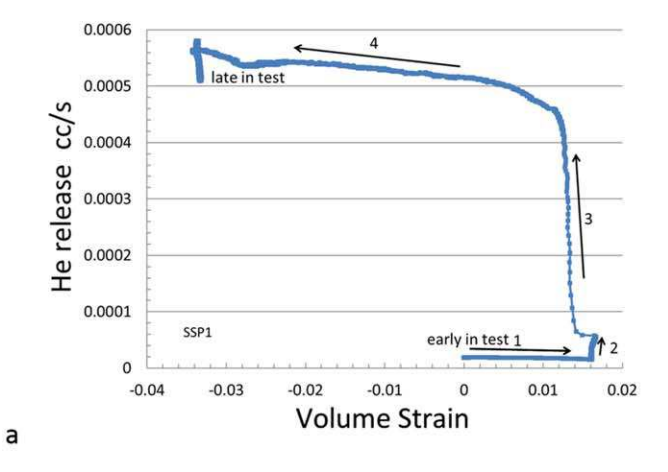
As deformation progresses, the increase in flow observed indicates microcracks are forming, facilitating helium release from the pore space (limb 2 on Figure 9). The increased helium release

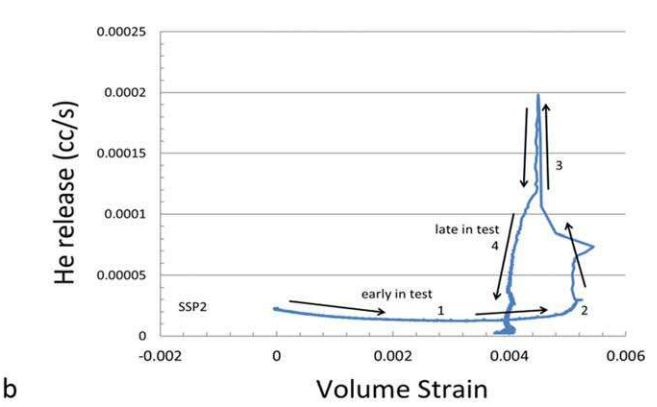
indicates that the microfracture network is pervasive enough to significantly enhance core-scale permeability before macroscopic dilatancy is observed. The helium release in advance of macroscopic failure may represent a laboratory example of that observed by *Padrón et al.* [2013]. They recorded an increase in the helium emission rate in advance of seismic energy releases associated with volcanic activity. Metamorphism and tectonic activity have been shown to release significant amounts of helium [*Lowenstern et al.*, 2014]. There appears to be a synergism of laboratory and field based studies relating helium release to deformation which can be exploited to elucidate operative processes and mechanisms.

A macrofracturing event follows the microfracture phase. During this phase helium release rapidly increases relative to volume strain (limb 3 in Figure 9). The abrupt increase in helium release indicates that throughgoing fractures have been formed, drastically increasing the permeability. The change in permeability and thus helium release is several orders of magnitude, whereas the change in volume strain is relatively small.

In most cases, macroscopic dilation follows, and dilation continues while the helium release drops. During this phase, the fracture has opened and further dilation does not result in a large increase in permeability or helium release. In SSP2 and SSP3, where the only reservoir of helium is within the rock core itself, a decrease in helium release is observed during this stage as the core helium reservoir is depleted. In SSP1, where an additional reservoir of helium was left on the upstream end of the core, we see constant flow as the upstream reservoir has not yet been depleted.

SSP2 shows a greater flow rate and drains faster (post failure) than SSP1 because the SSP2 specimen is connected to the mass spectrometer on both ends, and there is not an additional reservoir of helium in the volume of tubing between the sample and the upstream valve. The boundary conditions in SSP1 allow for a more complete interrogation of the fracture permeability, since there is more gas available to flow through





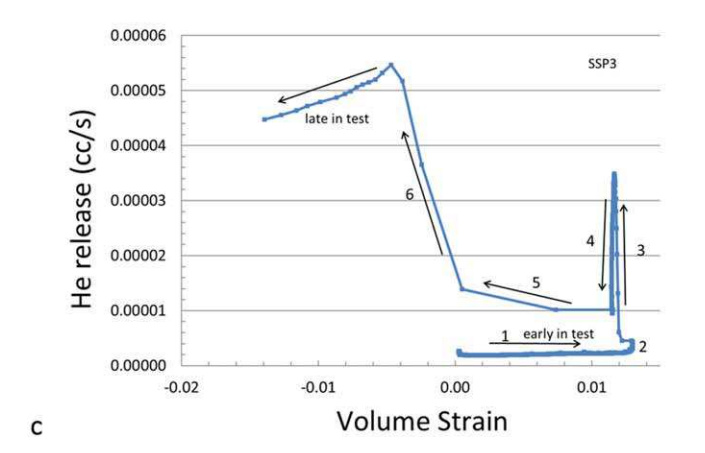


Figure 9. Volume strain versus helium release (a) SSP1, (b) SSP2, and (c) SSP3.

the fracture, while SSP2 gives more information on matrix transport to the fracture system, since there is no other reservoir of gas in that experiment.

Different fracture propagation characteristics produce different helium release signals. SSP1 and SSP2, are deformed parallel to bedding, and individual small-scale beds are in a constant-axial strain state. This concentrates stresses in the stiffer units, perhaps allowing microcracking and pore collapse to initiate/combine at to increase flow appropriate stress levels. This process could explain flow increases in advance of macroscopic volume strain increase.

For both SSP1 and SSP2, the flow rate increases dramatically with macrofracture. Cross cut sections through the specimens show that the fractures propagate along the entire length of the core. These macrofractures provide an ample conduit(s) which transect bedding, creating a preferential flow path, and results in a single large helium release event.

SSP3 is deformed perpendicular to bedding, and the individual smallscale beds are in a constant-axialstress state. This concentrates strain in the softer units and inhibits fracturing in the direction of flow. The flow rates and fracture release rates are lower in SSP3 than in SSP1 and SSP2, consistent with background permeability and fracture permeability being lower perpendicular to bedding. As deformation progresses, enough modification of the pore structure takes place to release helium from storage and cause a slow increase in flow during the compressional phase. It appears

that microfracturing is still significant enough to cause a sharp increase in helium release at the end of the compressional phase. In SSP3, we observe two smaller fracturing events, with smaller strains than in SSP1 and SSP2. This corresponds to two smaller helium release events in the helium flow signal.

#### 5. Conclusions

This scoping study presents experimental results which relate key dependent parameters, flow rate and volume strain, in a shale during triaxial deformation. We present the first continuous measurements of helium gas released from a shale during mechanical deformation. The helium release is sensitive to structural evolution of the sample during deformation and can be used to infer some of the major

processes occurring throughout deformation. A common pattern is seen in the responses, which show an initial compression phase during which axial strain increases and helium release steadily decreases. The compressional phase is followed by a microstructural deformation phase during which the permeability of the sample increases due to microscopic deformation before macroscopic dilation is observed. During this phase, the helium release rate from the core increases even as the sample continues to show macroscopic volume compression. During fracturing the helium flow rate rapidly peaks, followed by a monotonic decrease in flow. The helium release signal is sensitive to the details of the mechanical deformation and can provide information on changes in permeability, as well as the stress and strain states in shales and other rocks.

Helium and other noble gases contained in rock have the potential for release upon deformation. We have ongoing work on noble gas release in other rocks, and release timing relative to the imposed deformation. The release amount depends on the initial amount of gas, its location (pore, grain boundary, intragranular, etc.), and the imposed deformation. The cracks formed must intersect the gas host sites for it to be released. Other rocks that compact when deformed, for example, a poorly welded tuff, may show similar gas release response to shale, that is, gas release upon breaking/interconnecting gas containing pores. Low porosity crystalline igneous rock may not release gas until new intragranular cracks begin to form at half their yield strength. Young basalts may release gas at low stress levels when vesicles begin to fracture. Sandstones, if they contain noble gas in quartz grains, will release the gas as soon as grain contacts are sufficient to create transgranular microfractures.

This work sets the stage for monitoring the release of naturally occurring helium to infer changes in stress, strain, and permeability. Future work could include a systematic study on a single lithology where, for example, confining pressure is increased through the brittle ductile transition. As deformation becomes more pervasive, more gas should be released. Pressure sensitive deformation could be correlated to pressure sensitive flow characteristics of the deforming pore structure. Such experiments, coupled with detailed observation of operative processes at each step of the deformation, will provide insight into the relationship between flow and deformation of the rock. Quantitative interpretation of experiments of this kind could provide a basis for developing constitutive relationships between mechanical deformation and permeability and for using naturally occurring and doped tracers to observe and monitor mechanical deformation.

#### Acknowledgments

This work was funded under the Sandia Laboratory Directed Research and Development (LDRD) project 165670 and title "Appraisal of Hydraulic Fractures Using Natural Tracers." Data in plotted figures may be obtained from SJB upon request (sjbauer@sandia.gov). Sandia National Laboratories is a multiprogram laboratory managed and operated by Sandia Corporation, a wholly owned subsidiary of Lockheed Martin Corporation, for the U.S. Department of Energy's National Nuclear Security Administration under contract DE-AC04-94AL85000.

### References

- Bauer, S. J., M. Y. Lee, and W. P. Gardner (2015), Helium-mass-spectrometry-permeameter for the measurement of permeability of low permeability rock with application to triaxial deformation conditions, paper presented at 49th US Rock Mechanics/Geomechanics Symposium, Am. Rock Mech. Assoc., San Francisco, Calif., 28 June to 1 July.
- Bennett, R. H., K. M. Fischer, D. L. Lavoie, W. R. Bryant, and R. Rezak (1989), Porosimetry and fabric of marine clay and carbonate sediments: Determinants of permeability, *Mar. Geol.*, 89, 127–152.
- Brace, W. F. (1980), Permeability of crystalline and argillaceous rocks, Int. J. Rock Mech. Min. Sci. Geomech. Abstr., 17(5), 241–251.
- Dewers, T., J. Heath, R. Ewy, and L. Duranti (2012), Three-dimensional pore networks and transport properties of a shale gas formation determined from focused ion beam serial imaging, *Int. J. Oil Gas Coal Technol.*, 5(2/3), 229–248.
- Dewhurst, C. N., A. C. Aplin, J.-P. Sarda, and Y. Yang (1998), Compaction driven evolution of porosity and permeability in natural mudstones: An experimental study, *J. Geophys. Res.*, 103, 651–661.
- Dewhurst, C. N., A. C. Aplin, and J.-P. Sarda (1999), Influence of clay fraction on pore-scale properties and hydraulic conductivity of experimentally compacted mudstones, *J. Geophys. Res.*, 104, 261–274.
- Gardner, W. P., G. A. Harrington, and B. D. Smerdon (2012), Using excess <sup>4</sup>He to quantify variability in aquitard leakage, *J. Hydrol.*, 468, 63–75.
- Gutierrez, M., L. E. Øyno, and R. Nygärd (2000), Stress-dependent permeability of a de-mineralized fracture in shale, *Mar. Pet. Geol.*, 17, 895–907.
- Ikari, M. J., D. M. Saffer, and C. Marone (2009), Frictional and hydrologic properties of clay-rich fault gouge, *J. Geophys. Res.*, 114, B05409, doi:10.1029/2008JB006089.
- Katsube, T. J., B. S. Mudford, and M. E. Best (1991), Petrophysical characteristics of shales from the Scotian Shelf, *Geophysics*, *56*, 1681–1689.
- King, G. E. (2010), Thirty years of gas shale fracturing: What have we learned?, paper SPE 133456 presented at SPE Annual Technical Conference and Exhibition, Soc. of Pet. Eng., Florence, Italy.
- Kwon, O., A. K. Kronenberg, A. F. Gangi, B. Johnson, and B. E. Herbert (2004), Permeability of illite-bearing shale: 1. Anisotropy and effects of clay content and loading, *J. Geophys. Res.*, 109, B10205, doi:10.1029/2004JB003052.
- Loucks, R. G., R. M. Reed, S. C. Ruppel, and D. M. Jarvie (2009), Morphology, genesis, and distribution of nanometer-scale pores in siliceous mudstones of the Mississippian Barnett Shale, *J. Sediment. Res.*, 79(12), 848–861.
- Lowenstern, J. B., W. C. Evans, D. Bergfeld, and A. G. Hunt (2014), Prodigious degassing of a billion years of accumulated radiogenic helium at Yellowstone, *Nature*, 506, 355–358.

- Metwally, Y. M., and C. Sondergeld (2011), Measuring low permeabilities of gas-sands and shales using a pressure transmission technique, Int. J. Rock Mech. Min. Sci., 48(7), 1135–1144, doi:10.1016/j.ijrmms.2011.08.004.
- Morrow, C. A., L. Q. Shi, and J. D. Byerlee (1984), Permeability of fault gouge under confining pressure and shear stress, *J. Geophys. Res.*, 89, 3193–3200.
- Nicolas, A., F. Girault, A. Schubnel, É. Pili., F. Passelègue, J. Fortin, and D. Deldicque (2014), Radon emanation from brittle fracturing in granites under upper crustal conditions, *Geophys. Res. Lett.*, 41, 5436–5443, doi:10.1002/2014GL061095.
- Padrón, E., N. M. Pérez, P. A. Hernández, H. Sumino, G. V. Melián, J. Barrancos, and D. Nolasco (2013), Diffusive helium emissions as a precursory sign of volcanic unrest, *Geology*, 41, 539–542.
- Popp, T., and K. Salzer (2007), Anisotropy of seismic and mechanical properties of Opalinus clay during triaxial deformation in a multi-anvil apparatus, *Phys. Chem. Earth*, 32(8–14), 879–888, doi:10.1016/j.pce.2006.04.022.
- Slatt, R. M., and Y. Abousleiman (2011), Merging sequence stratigraphy and geomechanics for unconventional gas shales, *Leading Edge*, 30(3), 274–282.
- Sone, H. (2012), Mechanical properties of shale gas reservoir rocks and its relation to the in situ stress variation observed in Shale Gas Reservoirs, PhD dissertation, Stanford Univ.
- Tuccimei, P., S. Mollo, S. Vinciguerra, M. Castelluccio, and M. Soligo (2010), Radon and thoron emission from lithophysae-rich tuff under increasing deformation: An experimental study, *Geophys. Res. Lett.*, *37*, L05305, doi:10.1029/2009GL042134.
- Vermylen, J. P. (2011), Geomechanical studies of the Barnett Shale, Texas, USA, PhD dissertation, Stanford Univ.
- Yunlai, Y., and A. C. Aplin (2010), A permeability-porosity relationship for mudstones, Mar. Pet. Geol., 27(2010), 1692-1697.
- Zhang, C. L., and T. Rothfuchs (2008), Damage and sealing of clay rocks detected by measurements of gas permeability, *Phys. Chem. Earth*, 33(2008), 363–373.